Mechanism and control parameters of the coupled structural and metal-insulator transition in nickelates

Oleg E. Peil,[1,2] Alexander Hampel,[3] Claude Ederer,[3] and Antoine Georges[2,4,5,6]
[1]*Materials Center Leoben Forschung GmbH, Roseggerstraße 12, 8700 Leoben, Austria*
[2]*DQMP, Université de Genève, 24 quai Ernest Ansermet, 1211 Genève, Switzerland*
[3]*Materials Theory, ETH Zürich, Wolfgang-Pauli-Strasse 27, 8093 Zürich, Switzerland*
[4]*Collège de France, 11 place Marcelin Berthelot, 75005 Paris, France*
[5]*Center for Computational Quantum Physics, Flatiron Institute, 162 Fifth Avenue, New York, New York 10010, USA*
[6]*CPHT, Ecole Polytechnique, CNRS, Université Paris-Saclay, 91128 Palaiseau, France*

(Received 19 September 2018; revised manuscript received 12 February 2019; published 12 June 2019)

Rare-earth nickelates exhibit a remarkable metal-insulator transition accompanied by a symmetry-lowering structural distortion. Using model considerations and first-principles calculations, we present a theory of this phase transition which reveals the key role of the coupling between electronic and lattice instabilities. We show that the transition is driven by the proximity to an instability towards electronic disproportionation which couples to a specific structural distortion mode, cooperatively driving the system into the insulating state. This allows us to identify two key control parameters of the transition: the susceptibility to electronic disproportionation and the stiffness of the lattice mode. We show that our findings can be rationalized in terms of a Landau theory involving two coupled order parameters, with general implications for transition-metal oxides.

DOI: 10.1103/PhysRevB.99.245127

I. INTRODUCTION

The coupling of electrons to lattice degrees of freedom provides a key opportunity to control the properties of strongly correlated materials as in, e.g., epitaxial heterostructures [1]. Such a coupling often leads to concomitant electronic and structural transitions, which have been observed in V_2O_3 [2], manganates [3], Ca_2RuO_4 [4,5], etc. Rare-earth nickelates (RNiO$_3$) [6–8] represent an ideal playground in this respect because their metal-insulator transition (MIT), tightly associated with a lattice mode, is easily tunable [9,10].

The MIT in RNiO$_3$ is accompanied by a bond disproportionation (BD), i.e., a coherent contraction of the NiO_6 octahedra on one sublattice [short-bond (SB) octahedra] and an expansion of the octahedra on the other sublattice [long-bond (LB) octahedra], also referred to as the "breathing mode" (BM) [7,11]. The resulting "bond-disproportionated insulator" (BDI) is also characterized by an electronic disproportionation (ED), whereby the local configuration of SB octahedra is close to $d^8\underline{L}^2$ and that of LB octahedra is close to d^8 [12–15], or, in terms of "frontier" e_g orbitals, to e_g^0 and e_g^2, respectively [16–19]. The electron localization on the LB sublattice is the result of a "site-selective Mott transition" [20], occurring irrespective of the (ground-state) magnetic ordering for all systems with R cations smaller than Nd, and lowering the energy of the insulating phase below that of the metallic phase [14,21–23]. Therefore, magnetic order seems to play only a secondary role for the smaller R cations from Lu to Sm, enhancing an already existing tendency towards the MIT [24–26].

The mechanism of the interplay between electronic and lattice degrees of freedom is not yet understood. This question is of key importance to identify the driving force responsible for the BD and for the first-order transition [27] into the paramagnetic insulating state. This transition was previously described either as a pure charge-order transition [28] or as a result of only the coupling between lattice modes [29]. Recently, the authors of Ref. [30] proposed that the transition corresponds to the gradual softening of the BM, associated with the opening of a Peierls gap at the Fermi level, where they used density functional theory (DFT) calculations including the $+U$ correction. This theory describes the transition as second order, contradicting the results of the differential scanning calorimetry which provide clear evidence of the first-order transition [27]. The theory also contradicts Raman-spectroscopy studies revealing no hint of the BM softening [31]. Furthermore, the obtained band structure is not compatible with observed optical spectra of nickelates [32,33]. In addition, it cannot describe the MIT into the paramagnetic state since DFT + U requires a magnetically ordered state to produce an insulating gap [34,35]. Crucially, in the absence of magnetic ordering, the Peierls gap does not open at the Fermi level [17,33] and cannot thus be responsible for the insulating nature of the paramagnetic phase.

Here, we present a theory describing specifically the interplay between the electronic and structural aspects of the paramagnetic MIT found for R = Lu to Sm. We show that the paramagnetic MIT is driven by the proximity to a spontaneous ED, which leads to a strongly nonlinear electronic response with respect to variations of the BM amplitude, resulting in a first-order phase transition. Furthermore, we show that this nonlinear behavior and the first-order nature is key for a correct description of the paramagnetic MIT and obtaining a finite, stable-equilibrium BM amplitude. Moreover, our

theory also identifies the BM stiffness and the electronic susceptibility at $\mathbf{q} = (\frac{1}{2}, \frac{1}{2}, \frac{1}{2})$ as key parameters controlling the transition. Experimentally, these parameters can be tuned by the choice of the R cation [6] or by epitaxial strain in thin films and heterostructures [9,10,36]. We validate our theory by performing combined DFT and dynamical mean-field theory (DMFT) [37,38] calculations, allowing us to explore the trends across the rare-earth series. We also rationalize the overall physical picture in terms of a Landau theory involving two coupled order parameters: the ED and an order parameter associated with the metallicity of the system.

The paper is organized as follows. First, in Sec. II we introduce the model description and analyze its behavior by identifying control parameters of the coupled transition. Next, in Sec. II we verify these findings with our realistic DFT + DMFT calculations. Finally, in Sec. IV, we present a Landau theory rationalizing our findings further, and in Sec. V, we summarize our main results.

II. MODEL DESCRIPTION

We start by constructing a simplified model which reproduces the main features of the MIT in $R\mathrm{NiO_3}$. The model retains only the key low-energy degrees of freedom: the interacting electrons in the two frontier e_g orbitals and the BM amplitude Q. The purely electronic part of the Hamiltonian, $H_{\mathrm{band}} + H_{\mathrm{int}}$, consists of a simplified tight-binding (TB) model, $H_{\mathrm{band}} = -\sum_{i,j,m,m',\sigma} t_{ij}^{mm'} d_{im\sigma}^{\dagger} d_{jm\sigma}$, and a local interaction term H_{int}. Here, i, j indicate sites within a simple cubic lattice, $m = 1, 2$ correspond to the $d_{x^2-y^2}$ and d_{z^2} orbitals on each site, and hopping matrices $t_{ij}^{mm'}$ are obtained using the Slater-Koster construction with two hopping amplitudes, t and t', limited to nearest-neighbor and next-nearest-neighbor sites, respectively [39]. The interaction term H_{int} involves two coupling constants, a repulsive interaction U and an intra-atomic (Hund's) exchange J, and takes the standard two-orbital Hubbard-Kanamori form [40]. The purely lattice part is described by an elastic term: $H_{\mathrm{latt}} = \frac{K}{2} Q^2$, with K being the stiffness of the BM. Finally, importantly, the coupling of the BM amplitude to the electrons is captured by the term

$$H_{\mathrm{e-l}} = \frac{1}{2} \sum_{m\sigma} \Delta_m^s[Q] \left[\sum_{i \in \mathrm{SB}} \hat{n}_{im\sigma} - \sum_{i \in \mathrm{LB}} \hat{n}_{im\sigma} \right], \tag{1}$$

where $\hat{n}_{im\sigma} = d_{im\sigma}^{\dagger} d_{im\sigma}$ is the electron occupation operator and $\Delta_m^s[Q]$ is a (Peierls-like) modulation of the on-site potential seen by orbital m due to the BM structural distortion parametrized by Q. It couples to the operator measuring the ED between the LB and SB octahedra. The total Hamiltonian thus reads

$$H = H_{\mathrm{band}} + H_{\mathrm{int}} + H_{\mathrm{e-l}} + H_{\mathrm{latt}}. \tag{2}$$

At this stage, we define the amplitude Q as the disproportionation in octahedral bond lengths, $b = b_0 + Q/2$ for LB and $b = b_0 - Q/2$ for SB octahedra. The modulation of the on-site potential $\Delta_m^s[Q]$ is given by the difference between the on-site energies of the SB and LB sites:

$$\begin{aligned} \Delta_m^s[Q] &= \varepsilon_m[b_0 - Q/2] - \varepsilon_m[b_0 + Q/2] \\ &\approx (d\varepsilon_m/db)_{b_0} Q \equiv g_m Q, \end{aligned} \tag{3}$$

where we have expanded in Q and introduced the electron-lattice coupling parameter g_m. Here, we assumed that $\Delta_m^s[Q]$ is linear in Q, which we checked by our DFT calculations for various representatives of the series (see Fig. 6 in Appendix A).

As emphasized in Refs. [17,18], an appropriate low-energy description of the negative-charge-transfer character of $R\mathrm{NiO_3}$ and of their tendency to form a BDI state is obtained with $U - 3J \lesssim \Delta_s$. In this regime, the orbital polarization is strongly suppressed, implying that the on-site energies are, to a good approximation, orbital independent: $\varepsilon_{z^2} \approx \varepsilon_{x^2-y^2}$. We thus assume that the e_g states are degenerate and omit the index m in one-electron quantities (i.e., $g_m = g$, $\Delta_m^s = \Delta_s$) [41].

Minimizing the total energy,

$$E = \langle H \rangle \equiv E_{\mathrm{el}}[\nu] - \frac{gQ\nu}{2} + \frac{KQ^2}{2}, \tag{4}$$

with respect to Q (using the Hellman-Feynman theorem) yields

$$\frac{2K}{g} \bar{Q} = \nu[\bar{Q}], \tag{5}$$

where $\nu[Q] = \langle \hat{n}_{\mathrm{LB}} - \hat{n}_{\mathrm{SB}} \rangle_Q$ is the average ED for a given amplitude Q, while $\bar{Q}$ denotes the equilibrium value of the amplitude corresponding to local energy minima (solutions corresponding to energy maxima are discarded). Equation (5) is the central equation of this paper: It enables one to determine the equilibrium BM amplitude from the knowledge of the electronic response encoded in $\nu[Q]$ for a given lattice stiffness K and electron-lattice coupling g. The stability of the solutions of this equation is determined by the renormalized stiffness

$$\kappa \equiv \frac{\partial^2 E}{\partial Q^2} = K - \frac{g^2}{2} \frac{\partial \nu}{\partial \Delta_s}. \tag{6}$$

Assuming no spontaneous ED ($\nu[Q = 0] = 0$), we obtain $\kappa = K - \chi_e g^2/2$, where $\chi_e \equiv (\partial \nu / \partial \Delta^s)_{Q=0}$ is the electronic susceptibility associated with a "charge" modulation at a wave vector $\mathbf{q} = (\frac{1}{2}, \frac{1}{2}, \frac{1}{2})$ (see Appendix A 3 for more information). Hence, the (linear) stability of the high-symmetry phase is controlled by the electronic response χ_e which must be compared to $2K/g^2$.

We investigate the solutions to Eq. (5) by performing DMFT calculations to obtain $\nu[Q]$ for various values of the bandwidth W (see Appendix A 4 for details). The results are shown in Fig. 1. The calculations were performed first for increasing values and then for decreasing values of Q, which resulted in a hysteresis. The most important feature of this plot is the strongly nonlinear dependence of ν on Q. Solutions of Eq. (5) are obtained by intersecting $\nu[Q]$ with the straight line $(2K/g)Q$.

This nonlinear shape of the $\nu[Q]$ curves plays an important role in determining the nature of the transition. For a given value of K/g and depending on W, there are either one, two, or three intersection points (disregarding symmetry-equivalent solutions for $Q < 0$). Consider $K/g = 5.3$ Å^{-1}. If W is large ($W \geqslant 2.07$ eV in Fig. 1), the straight line intersects the ED curve only at $Q = 0$, rendering it the only solution to Eq. (5). As W is decreased, it reaches a value below which there are

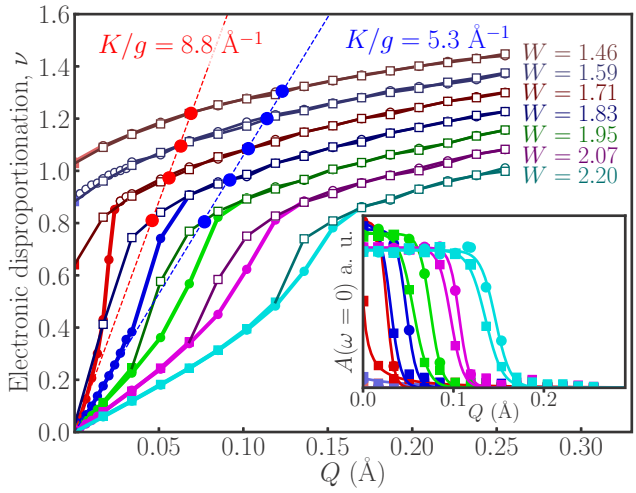

FIG. 1. Electronic disproportionation ν of the TB model as a function of bond disproportionation Q for various values of the bandwidth W (in eV). Open and solid symbols correspond to insulating and metallic branches, respectively. The dashed lines represent $(2K/g)Q$ for two values of K/g, with the intersection points giving the solutions to Eq. (5). Inset: Spectral weight as a function of Q.

three intersection points ($W = 1.95$ eV). The middle intersection point corresponds to an unstable solution ($\kappa < 0$). The two remaining stable solutions, $Q = 0$ and $Q = \bar{Q}[K, W] > 0$, mark the coexistence of two different phases. At even smaller values of W ($W \lesssim 1.8$) the solution at $Q = 0$ gets destabilized because $\kappa[Q = 0] < 0$. We are then left with only one solution, $Q = \bar{Q}[K, W] > 0$, telling us that only the BD phase is stable here. The behavior of the solutions of Eq. (5) as a function of W tells us that the BD transition is first order. Importantly, this is not directly related to the hysteretic behavior of $\nu[Q]$. Even if there were no such hysteresis, the particular nonlinear dependence of $\nu[Q]$ would imply that the BD transition is first order. The inset of Fig. 1 displays the spectral weight at the Fermi level as a function of Q. We see that the system undergoes a transition from metallic to insulating behavior as Q is increased and that the transition regime corresponds to the strongly nonlinear regime of $\nu[Q]$. Hence, it is the MIT which is responsible for the strong nonlinearity of $\nu[Q]$.

We can now discuss the control parameters of the combined BD/MIT, where Eq. (5) shows that the transition behavior depends on parameters g, K, and χ_e. We extract these parameters from our DFT calculations (see Appendix A 2 for details), and the obtained values for g, K, their ratios, χ_e, and the e_g bandwidth W are shown in Table I. To get a better feel for these numbers, one can estimate the maximum possible equilibrium BM amplitude by setting $\nu = 2$ in Eq. (1), which yields $\bar{Q}_{\max} = 2(g/2K) \approx 0.095$ Å, a value that sets the correct scale of distortions observed in experiment (e.g., $\bar{Q} = 0.075$ Å for $LuNiO_3$). This provides a strong argument in favor of the presented mechanism of the electron-lattice coupling as the dominant one in determining the structural transition.

The electron-lattice coupling g is found to vary by about 12% along the rare-earth series. Moreover, the stiffness K also varies by a similar amount and in the same direction (increasing from Lu to Sm). As a result, the ratio $2K/g$, which enters the equation of state, is fairly constant along the series. The renormalized stiffness controlling the sensitivity to disproportionation at small Q is proportional to $2K/g^2 - \chi_e$, with χ_e being the electronic susceptibility. From Table I it can be seen that the first term varies by about 10% along the series, but the electronic susceptibility varies by almost a factor of 2 from Pr to Lu. As a result, for the bulk materials, the transition is sensitively controlled by the electronic susceptibility (i.e., by the bandwidth and rotation and tilt angles [28]) and not by the stiffness K or electron-lattice coupling g. In heterostructures and under strain, the BM stiffness K varies, while g remains unaffected [36]. K is thus likely to be an important control parameter in those cases. This may shed light on the results of Ref. [42] and motivates the variation of K/g in our model calculations.

TABLE I. Values for g, K, $2K/g$, $2K/g^2$, the e_g bandwidth W, and the $d_{x^2-y^2}$ component of the electronic susceptibility $\chi_{1,1}$ for the three investigated compounds R = Lu, Sm, and Pr, extracted from DFT calculations.

R	g (eV/Å)	K (eV/Å^2)	$2K/g$ (1/Å)	$2K/g^2$ (1/eV)	W (eV)	$\chi_{1,1}$ (1/eV)
Lu	3.75	39.29	20.96	5.59	2.32	0.69
Sm	4.02	41.45	20.61	5.13	2.51	0.50
Pr	4.24	44.47	20.98	4.95	2.68	0.39

The effects of the two control parameters K and χ_e (tuned via K/g and W, respectively) are summarized in Fig. 2. The dashed curves indicate the boundaries (spinodals) of the BDI and metallic phases, with a narrow coexistence region in between. Solid lines show stable nonzero solutions $\bar{Q}[K, W]$. For fixed K, the bandwidth W (equivalently, χ_e) determines

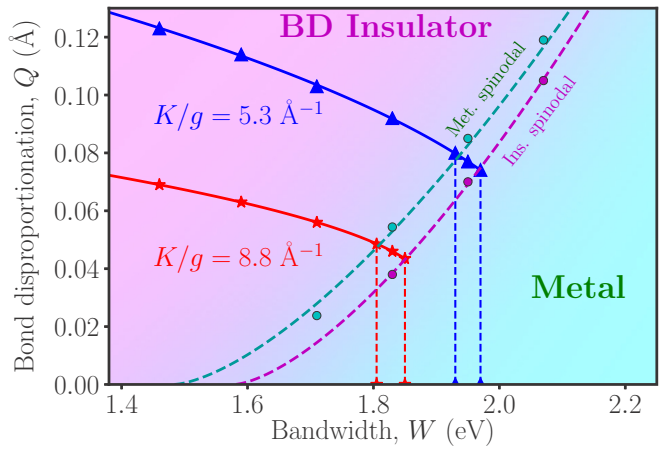

FIG. 2. Phase diagram of the TB model as a function of bandwidth W and BD Q. Circles are critical points for the metallic and insulating phases; dashed curves are spinodal lines obtained as fits to $\alpha(W - W_c)^{\frac{3}{2}}$ (see Sec. IV on the Landau theory). The solid lines with triangles and stars display the stable equilibrium values of Q for two values of K/g. Vertical dashed lines designate lower and upper critical values of W for the structural transition.

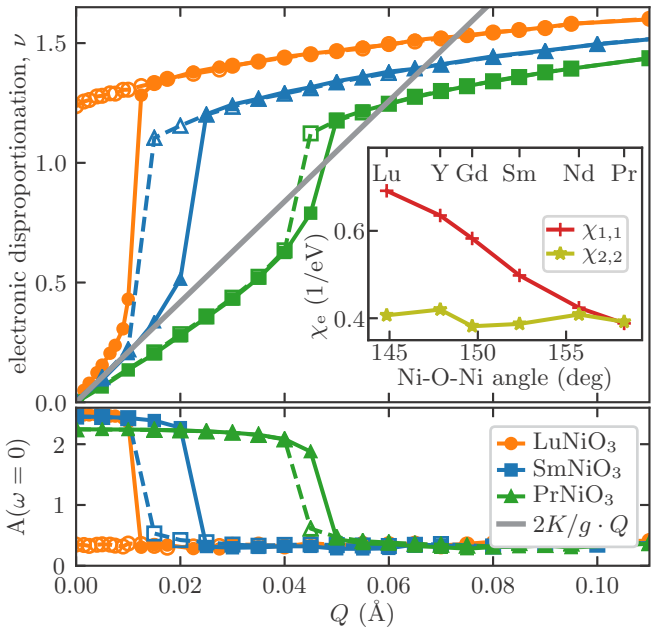

FIG. 3. Top: ED ν as a function of increasing Q (solid symbols) and decreasing Q (open symbols) for $R =$ Lu (red), Sm (blue), and Pr (green). The gray line represents $(2K/g)Q$ with values $g = 3.8$ eV/Å and $K = 39.3$ eV/Å^2 extracted from DFT. Inset: Electronic susceptibilities as a function of the Ni-O-Ni angle: $\chi_{1,1}$ is the $d_{x^2-y^2}$ component, and $\chi_{2,2}$ is the d_{z^2} component. Bottom: spectral weight at the Fermi level as a function of Q.

whether the paramagnetic ground state is a BDI phase. Moreover, the variation of K controls smoothly the position of the phase boundaries.

III. REALISTIC DFT + DMFT CALCULATIONS

We now perform *ab initio* DFT + DMFT calculations to confirm the physics found in the model calculations and assess materials trends quantitatively. The impurity model is constructed by projecting onto a low-energy e_g subspace following the scheme described in Refs. [17,18] (see Appendix A 4 for details).

Figure 3 shows the calculated $\nu(Q)$ for $R =$ Lu, Sm, and Pr (top panel). The overall nonlinear behavior of $\nu(Q)$ is very similar to that in the model calculations (Fig. 1), with the nonlinearity clearly related to the MIT (Fig. 3, bottom panel), also indicating a first-order character of the BD/MIT. This confirms that the model indeed incorporates the essential underlying physics. Furthermore, we obtain a strong decrease in the amplitude of the nonlinearity in $\nu(Q)$ from $R =$ Lu towards $R =$ Pr, consistent with the bandwidth variation in the model.

For the realistic calculations, we checked the change in bandwidth W for different R cations obtained by DFT. The corresponding values of W for $R =$ Lu, Sm, and Pr are shown in Table I (see also Fig. 5 in Appendix A). One can see that the bandwidth decreases by ~13% from $R =$ Pr to $R =$ Lu. On the other hand, the $d_{x^2-y^2}$ component of the electronic susceptibility displayed in Fig. 3 (top, inset) increases steadily and almost doubles its value from Pr to Lu as the Ni-O-Ni bond angle is reduced. Together, this shows that the increased octahedral rotations for $R =$ Lu compared to $R =$ Pr have a much stronger impact on the electronic susceptibility χ_e than on the bandwidth W. This effect can be understood by realizing that the bandwidth is mainly determined by the nearest-neighbor hopping parameter t, while the susceptibility is also crucially dependent on the next-nearest-neighbor hopping parameter t' (more precisely, on the ratio t'/t), affecting the shape of the Fermi surface [28,39]. The bandwidth provides thus only an indirect measure of the changes in the true control parameter χ_e determining the proximity to the instability.

Finally, the values obtained for K and g from DFT (see Table I) lead to stable equilibrium BM amplitudes $\bar{Q}$ for all investigated compounds. This is shown in Fig. 3, where $\bar{Q}$ is obtained from the crossing points of $(2K/g)Q$ (gray line) with the $\nu[Q]$ curves. The value obtained for $\bar{Q}$ for $LuNiO_3$ of 0.073 Å is in very good agreement with available experimental data ($Q_{exp} = 0.075$ Å [27]). $PrNiO_3$ seems to be very close to the transition, as its $\bar{Q}$ value is very close to the MIT, and the stable BM would eventually be lost if a reduced U were used for $PrNiO_3$, as suggested by our constrained random-phase approximation calculations [22]. Moreover, previous studies find that the magnetic order appears to be crucial in stabilizing the BD phase in $PrNiO_3$ and $NdNiO_3$ [7,22,24,25]. The stability and influence of the magnetic order goes beyond the scope of our work and requires further investigation. However, the overall trend of an increase in Q and in the stability of the BM through the series for smaller R cations is consistent with experiments and in line with earlier studies [19,22,35]. Moreover, these results clearly show the capabilities of the method to correctly capture the coupled paramagnetic MIT and the resulting stability of the BM distortion compared to a DFT + U description.

IV. LANDAU THEORY

We finally show that the main qualitative features of the MIT found above can be rationalized in terms of a Landau theory, which involves two coupled scalar order parameters: the ED ν and an additional order parameter, ϕ, which distinguishes between metallic (conventionally associated with $\phi > 0$) and insulating behavior ($\phi < 0$). The reason why this second-order parameter is required is clear from the results above: a nonzero value of ν can correspond either to a metallic phase (at small values of the on-site modulation Δ_s or, equivalently, of Q) or to an insulating one. In other words, a metallic monoclinic phase with a nonzero value of the BM amplitude Q is, in principle, possible, in agreement with recent experimental findings [43]. Such an order parameter has been introduced to describe the Mott transition in the DMFT framework, in analogy with the liquid-gas transition [44,45]. Note that the present Landau theory aims at describing the MIT between the two paramagnetic phases, while the earlier Landau descriptions [24,39] aimed at the magnetic transition (see also Ref. [5] in relation to ruthenates.)

Assuming the simplest coupling allowed by symmetry, $\phi\nu^2$, the paramagnetic transitions can be described by the following energy functional:

$$F[\nu, \phi] = F_\nu + F_\phi + \lambda\phi\nu^2, \tag{7}$$

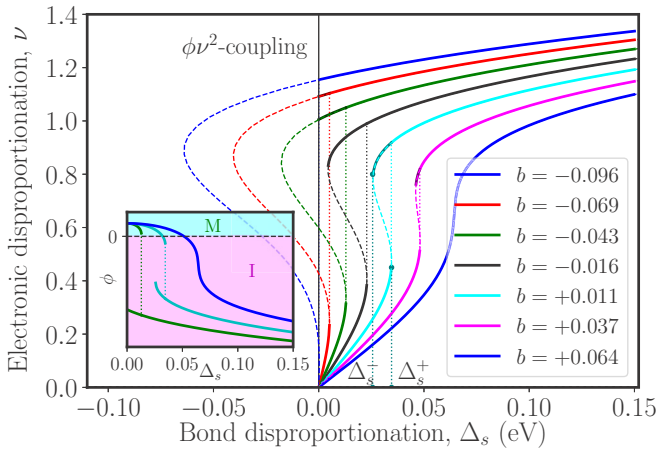

FIG. 4. ED ν as a function of Δ_s for various values of parameter b, as obtained within the Landau theory described in the text. Dashed lines display unstable solutions. Critical points Δ_s^-, Δ_s^+ are indicated for one of the cases. Inset: MI order parameter ϕ as a function of Δ_s for three selected cases ($b = -0.043$, 0.011, 0.064). The region marked M shows the metallic phase ($\phi > 0$); the region marked I shows the insulating phase ($\phi < 0$).

with

$$F_\nu = \tfrac{1}{2}b\nu^2 + \tfrac{1}{4}c\nu^4 - \Delta_s\nu + \tfrac{1}{2}\kappa\Delta_s^2,$$
$$F_\phi = \tfrac{1}{2}a\phi^2 + \tfrac{1}{4}u\phi^4 - h\phi, \tag{8}$$

where $u, c > 0$ and the coupling parameter $\lambda > 0$ is of order 1. The coupling to the lattice is represented by the linear term $\Delta_s\nu$, with Δ_s serving as a symmetry-breaking field (alternatively, the BM can be introduced with $Q = g\Delta_s$). In the absence of ED, the system is a metal, so that we must assume a and h are positive. Here, b is a key control parameter related to χ_e, and it depends critically on external parameters such as the bandwidth, $b = b_0(W - W_c)$.

Without loss of generality we can set $u = c = a = 1$. Minimizing $F[\nu, \phi]$ yields the following coupled equations of state:

$$b\nu + \nu^3 + 2\lambda\phi\nu = \Delta_s, \tag{9}$$

$$\phi + \phi^3 = h - \lambda\nu^2. \tag{10}$$

The numerical solution of these equations is displayed in Fig. 4 for various b. For $b > 0$, starting from a value $\phi = \phi_0 > 0$, typical for the metallic phase at $\nu = 0$, and increasing Δ_s lead to a strongly nonlinear dependence of ν on Δ_s, with ϕ continuously decreasing (because of the $-\lambda\nu^2$ term) and gradually reaching negative values (inset of Fig. 4). At a critical value of b, the $\nu[\Delta_s]$ curves acquire a vertical tangent, and beyond this value, an S shape with an unstable branch is found, typical of a first-order transition, with two vertical tangents delimiting the two spinodal values of Δ_s: Δ_s^- and Δ_s^+. When b is further decreased, a spontaneous instability is found, with a jump of ν to a finite value for an infinitesimal Δ_s. This general behavior is in excellent qualitative agreement with Fig. 1.

A more detailed analysis of the above equation can be carried out by considering two limits: small and large values of Δ_s. The small-Δ_s limit can be described in terms of the linear susceptibility at $\nu = 0$, $\chi_e = (b + 2\lambda\phi_0)^{-1}$, associated with the electronic disproportionation. Keeping terms up to $O(\Delta_s^2)$, we can get the nonlinear susceptibility (see Appendix B for details),

$$\frac{d\nu}{d\Delta_s} = \left[\chi_e^{-1} - S\chi_e^2\Delta_s^2\right]^{-1}, \tag{11}$$

where $S > 0$ is a constant enhancement factor proportional to λ^2. The equation emphasizes the role of the $\phi\nu^2$ coupling in amplifying the electronic disproportionation, driving it to the transition at $\Delta_s = \Delta_s^+ \equiv (b + 2\lambda\phi_0)^{\frac{3}{2}}/\sqrt{S} \sim (W - W^+)^{\frac{3}{2}}$. At this point $d\nu/d\Delta_s$ diverges, marking the spinodal of the metallic phase.

Analogously, the analysis of the large-Δ_s limit reveals that also for the spinodal of the insulating phase we get $\Delta_s^- \sim (W - W^-)^{\frac{3}{2}}$ (details are given in Appendix B). The similar behaviors of the metallic and insulating spinodals are confirmed by the DMFT results for the TB model displayed in Fig. 1, where one can see that the two boundaries are fairly parallel.

V. CONCLUSIONS

We have presented a theory of the combined structural and electronic metal-insulator transition in bulk $R\mathrm{NiO}_3$. The driving force of this transition is the proximity to the electronic disproportionation instability, which is cooperatively reinforced by the coupling to the lattice breathing mode. The transition is thus controlled both by the electronic charge susceptibility and by the stiffness of this mode. The key nonlinearities associated with this cooperative effect can be rationalized in terms of a Landau theory. Our work provides a pathway to understanding the MIT in other geometries, such as ultrathin films and heterostructures, and is likely to have general applicability to other materials with a strong interplay between electronic correlations and lattice degrees of freedom.

ACKNOWLEDGMENTS

We are grateful to C. Ahn, D. Basov, J. Chakhalian, A. Georgescu, A. J. Millis, J. M. Triscone, and D. van der Marel for discussions. This work was supported by the European Research Council (Grant No. ERC-319286-'QMAC'), the Swiss National Science Foundation (NCCR MARVEL), and the Swiss National Supercomputing Centre (Projects No. s575, No. s624, No. mr17, and No. s820). The Flatiron Institute is a division of the Simons Foundation. O.E.P. gratefully acknowledges the financial support under the scope of the COMET program within the K2 Center "Integrated Computational Material, Process and Product Engineering (IC-MPPE)" (Project No. 859480). This program is supported by the Austrian Federal Ministry for Transport, Innovation and Technology (BMVIT) and Federal Ministry of Digital and Economic Affairs (BMDW), represented by the Austrian research funding association (FFG), and the federal states of Styria, Upper Austria, and Tyrol.

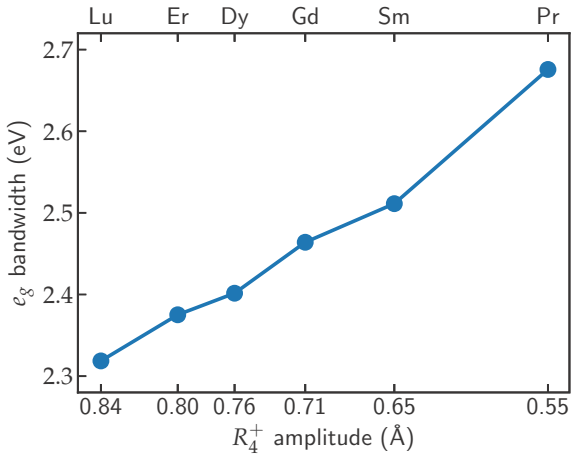

FIG. 5. Bandwidth W of the e_g bands as a function of rare-earth ion R obtained from DFT corresponding to the *Pbnm* structure ($Q = 0.0$ Å).

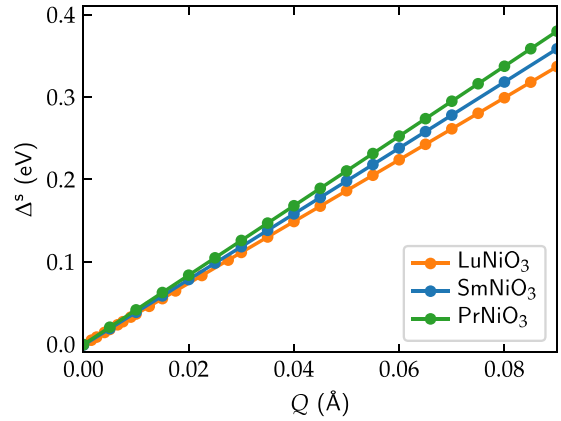

FIG. 6. $\Delta^s[Q]$ for R = Lu (red), Sm (blue), and Pr (green) as extracted from DFT. A clear linear dependency of $\Delta^s[Q]$ from Q can be observed for all three R cations.

APPENDIX A: CALCULATION DETAILS

1. DFT calculations

DFT calculations were performed using the projector augmented wave (PAW) method [46] implemented in the Vienna Ab initio Simulation Package (VASP) [47–49] and the exchange correlation functional according to Perdew, Burke, and Ernzerhof [50]. For Ni, the $3p$ semicore states were included as valence electrons in the PAW potential. For the rare-earth atoms, we used PAW potentials corresponding to a $3+$ valence state with f electrons frozen into the core, and depending on the rare-earth cation, the corresponding $5p$ and $5s$ states were also included as valence electrons. A k-point mesh with $10 \times 10 \times 8$ grid points along the three reciprocal lattice directions was used, and a plane wave energy cutoff of 550 eV was chosen for the 20-atom *Pbnm* unit cell. The structures were fully relaxed, both internal parameters and lattice parameters, until the forces acting on all atoms were smaller than 10^{-4} eV/Å. Generally, our calculated lattice parameters agree very well with available experimental data across the whole series, with maximal deviations of the unit cell volume of a few percent or less. For example, for $LuNiO_3$ the nonmagnetic calculation results in a unit cell volume that deviates by -1.5% from the experimental high-temperature structure [27]. As can be seen from Ref. [35], all rotation and tilt angles are also in very good agreement with the experimental structure.

To check the influence of the different control parameters across the nickelate series, we extracted the bandwidth W of the e_g states from our DFT calculations for the relaxed *Pbnm* structures, which is depicted in Fig. 5. Here, W is plotted as function of the octahedral rotation distortion amplitude R_4^+, which is related to the Ni-O-Ni super-exchange angle [35].

2. Electron-lattice coupling

We use slightly different definitions of the BM amplitude Q in the model and in the realistic calculations. In the model, Q is defined as the difference in bond lengths (oxygen-atom displacement is $\sim Q/2$), while in DFT + DMFT calculations, the BM amplitude corresponds to a particular distortion mode (R_1^+) of a symmetry-based mode decomposition [35,51,52]. Since the amplitude of this mode is proportional to the displacement of oxygen atoms, its value is almost a factor of 2 smaller than the model value of Q. More specifically, an amplitude of $Q = 0.1$ Å would result in a displacement of 0.058 Å of each oxygen atom. The decomposition in distortion modes allows us to clearly separate the effect of the BM from other distortions and hence allows for a better comparison with the model. As experiments show [27,53], structural parameters besides the breathing mode distortion almost do not change during the MIT, and therefore, the use of our relaxed *Pbnm* structures is well justified.

In the model calculations, $Q = \Delta_s/g$ is controlled by varying the modulation parameter Δ_s. The length scale is set by setting $g = 1.7$ eV/Å, which is close to $g_{\mathrm{DFT}}/2$, with g_{DFT} being the value obtained in our DFT calculations for bulk $R\mathrm{NiO_3}$ (see below). Model parameter K can be chosen rather arbitrarily, and we vary it in a range of values that results in equilibrium values of Q of the same order of magnitude as the experimentally observed values (and the ones resulting from DFT + DMFT calculations). Note that because of the difference in the definition of Q the model values of K would correspond to roughly four times larger values of the realistic BM stiffness.

In our realistic calculations, parameters g and K are determined from systematic DFT calculations for varying BM amplitude, where the modulation field Δ_s is extracted from the difference of the corresponding on-site terms of the Hamiltonian projected onto e_g states via Wannier construction as described in Refs. [54,55]. To this end, we use the TRIQS/DFTTOOLS software package [56,57]. The resulting values of Δ_s turn out to be linear in Q in the relevant range of BM amplitudes, as seen in Fig. 6, where we show several examples of such calculations. In the context of DFT + DMFT calculations, the value of Δ_s is corrected for the double-counting (DC) contributions as described in Ref. [18].

The obtained values of the parameters allow for an estimate of the relative strength of the electron-lattice coupling by considering a polaron binding energy $g^2/(2K)$, which is $E_p \approx 184$ meV for our obtained values g and K from DFT. The corresponding dimensionless coupling parameter is then equal

to $\lambda = E_p/W \approx 0.08 \ll 1$ for $LuNiO_3$ (it is even smaller for other compounds in the series), which tells us that electrons are coupled relatively weakly to the BM in nickelates. This emphasizes the key role that the electronic instability plays in effectively enhancing the coupling and destabilizing the BM.

3. Electronic susceptibility

Here, we show that the formula for the susceptibility given in the text is related to the usual definition of the charge susceptibility at a specific $\mathbf{q}$ point. If we consider an inhomogeneous perturbation potential of the form $H' = \sum_i \hat{n}_i \epsilon_i$ (again, assuming orbital degeneracy and omitting the orbital and spin indices), then the $\mathbf{q}$-dependent charge susceptibility is defined as

$$\chi(\mathbf{q}) = -\frac{\partial n(\mathbf{q})}{\partial \epsilon(\mathbf{q})}\Big|_{\epsilon\to 0}, \tag{A1}$$

with

$$n(\mathbf{q}) = \frac{1}{N}\sum_i \langle \hat{n}\rangle_i e^{i\mathbf{q}\mathbf{R}_i}, \quad \epsilon(\mathbf{q}) = \frac{1}{N}\sum_i \epsilon_i e^{i\mathbf{q}\mathbf{R}_i},$$

where $\mathbf{R}_i = m_i^1\mathbf{a}_1 + m_i^2\mathbf{a}_2 + m_i^3\mathbf{a}_3$ are the Bravais-lattice vectors, $\mathbf{a}_\alpha$ are the translation vectors of the pseudocubic unit cell, and $m_i^\alpha \in \mathbb{Z}$ ($\alpha = 1, 2, 3$).

Considering a modulated field ϵ_i equal to $\Delta_s/2$ on SB sites and to $-\Delta_s/2$ on LB sites, we have for a specific point $\mathbf{q}_R = \frac{2\pi}{a}(\frac{1}{2}, \frac{1}{2}, \frac{1}{2})$ in a pseudocubic structure

$$\begin{aligned} n(\mathbf{q}_R) &= \frac{1}{N}\sum_i \langle \hat{n}\rangle_i e^{i\pi(m_i^1+m_i^2+m_i^3)} \\ &= \frac{1}{N}\left(\sum_{i\in \mathrm{LB}}\langle \hat{n}\rangle_i - \sum_{i\in \mathrm{SB}}\langle \hat{n}\rangle_i\right) = \frac{1}{2}\nu \\ \epsilon(\mathbf{q}_R) &= \frac{1}{N}\sum_i \epsilon_i e^{i\pi(m_i^1+m_i^2+m_i^3)} \\ &= \frac{1}{N}\left(\sum_{i\in \mathrm{LB}}\epsilon_i - \sum_{i\in \mathrm{SB}}\epsilon_i\right) = -\frac{1}{2}\Delta_s, \end{aligned}$$

where we have associated LB and SB sites with the sites for which the values of $m_i = \sum_\alpha m_i^\alpha$ are even and odd, respectively.

Then, we get

$$\chi(\mathbf{q}_R) = \frac{\partial \nu}{\partial \Delta_s}\Big|_{\epsilon\to 0}, \tag{A2}$$

which is the definition of χ_e used in the main text.

4. DMFT calculations

DMFT calculations for the TB model Hamiltonian are performed in the paramagnetic state. The bandwidth is given by $W = 6.1t$, and the ratio, $t'/t = 0.13$, is fixed for all calculations. The interaction parameters are set to $U = 1.8$ eV, $J = 0.9$ eV, similar to what has been used for a realistic low-energy description of $RNiO_3$ [17,18]. The temperature is set to $T = 1/100$ eV $\simeq 120$ K. The DMFT calculations are performed using hybridization-expansion continuous-time quantum Monte Carlo [58], as implemented in the TRIQS package [57,59], with the rotationally invariant Kanamori-type interaction term.

Within the realistic DFT + DMFT framework, we solve the electronic problem defined by the lattice Hamiltonian, $\hat{H} = \hat{H}_{\mathrm{kin}} + \hat{H}_{\mathrm{int}} + \hat{H}_V$, utilizing the above-mentioned solver. Here, the first term in $\hat{H}$ corresponds to the full e_g bands extracted from DFT, including all off-diagonal hoppings and on-site terms; the second term is the local interaction Hamiltonian, where we use the rotationally invariant Kanamori form, and the last term describes the intersite Coulomb interaction V, as introduced in Ref. [18], which we include on a mean-field level as a Hartree shift in the local self-energy.

We perform one-shot DFT + DMFT calculations, but according to our test calculations (see also Ref. [22]), the incorporation of intersite interactions on a Hartree level within a one-shot DFT + DMFT scheme gives results that are very similar to fully charge self-consistent DFT + DMFT calculations using only the local interaction term.

To correct for the DC error, we employ the scheme described in Ref. [60], where we additionally perform a DC correction for the intersite interaction as described in Ref. [18]. For better comparability, we use the same interaction parameters, $U = 1.8$ eV, $J = 0.4$ eV, and $V = 0.6$ eV, for all compounds throughout the series. These values are close to the results of recent calculations using the constrained random-phase approximation [18,22]. All calculations are done for the paramagnetic phase, and the temperature was set to $T = 1/40$ eV $\simeq 290$ K.

APPENDIX B: LANDAU THEORY

Here, we elaborate on the derivation of the critical-point scaling mentioned in the main text. We start with the equations of state given by Eqs. (9) and (10) in the main text and consider separately metallic and insulating regimes.

Stability of the metallic phase. For the metallic regime, we perform derivation by expanding in the limit of small Δ_s. At $\nu = 0$, we set $\phi = \phi_0 > 0$ to make sure the system is metallic in the absence of BD.

The symmetry of the problem dictates that ν is an odd function and ϕ is an even function of Δ_s. To first order in Δ_s we get

$$\nu_0 \approx \chi_e \Delta_s, \tag{B1}$$

$$\chi_e = \frac{1}{b + 2\lambda\phi_0}, \quad b > -2\lambda\phi_0. \tag{B2}$$

This result is not very interesting because it implies a linear behavior of ν and a constant value of ϕ_0 as a function of Δ_s, with Δ_s having thus no effect on the metal-insulator order parameter. This excludes any transition induced by bond disproportionation, leaving only a simple externally driven transition when $b = 2\lambda\phi_0$.

To get the next leading order, let $\phi = \phi_0 + \phi_1$, which gives

$$\begin{aligned} (\phi_0 + \phi_1)^3 + (\phi_0 + \phi_1) &= h - \lambda\nu_0^2, \\ 3\phi_0^2\phi_1 + \phi_1 &\approx -\lambda\chi_e^2\Delta_s^2, \end{aligned}$$

where terms of order $o(\Delta_s^2)$ are dropped.

We obtain the following solution:

$$\phi_1 = -\frac{\lambda}{M}\chi_e^2\Delta_s^2, \quad M = 1 + 3\phi_e^2. \tag{B3}$$

Importantly, we see that $\phi_1 < 0$, and ϕ hence decreases quadratically with Δ_s (see the inset of Fig. 4). Moreover, the rate of the reduction is determined by the charge susceptibility χ_e and also by the strength ("conductivity") ϕ_0 of the metallic phase.

To estimate the dependence of the nonlinear susceptibility on Δ_s we take the derivatives of the equations of state, Eqs. (9) and (10), with respect to Δ_s. Denoting $\chi(\Delta_s) = \partial\nu/\partial\Delta_s$ and, again, keeping only terms up to $O(\Delta_s^2)$, we have

$$3\phi^2\frac{\partial\phi}{\partial\Delta_s} + \frac{\partial\phi}{\partial\Delta_s} = -2\lambda\nu\chi, \quad \frac{\partial\phi}{\partial\Delta_s} \approx -2\frac{\lambda}{M}\nu\chi, \tag{B4}$$

from which we have

$$\begin{aligned} 3\nu^2\chi + (b+2\lambda\phi)\chi + 2\lambda\nu\frac{\partial\phi}{\partial\Delta_s} &= 1, \\ \left(3\nu_0^2 + \chi_e^{-1} - 6\frac{\lambda^2}{M}\nu_0^2\right)\chi &= 1, \\ \chi_e^{-1} - 3\left(2\frac{\lambda^2}{M} - 1\right)\chi_e^2\Delta_s^2 &= \chi^{-1}, \end{aligned} \tag{B5}$$

where we have used Eqs. (B1), (B2), (B3), and (B4). The resulting equation is precisely our Eq. (11) in the main text, with $S = 3(2\lambda^2/M - 1)$.

The function $\chi(\Delta_s)$ is equal to χ_e at $\Delta_s = 0$, increases with Δ_s faster than $\chi_e\Delta_s$, and diverges when $\Delta_s = \Delta_s^+$, with

$$\Delta_s^+ = \frac{\chi_e^{-\frac{3}{2}}}{\sqrt{S}}. \tag{B6}$$

The important observation here is that

$$\Delta_s^+ \sim (b + 2\lambda\phi_0)^{\frac{3}{2}} \sim (W - W^+)^{\frac{3}{2}}, \tag{B7}$$

which is exactly the scaling employed in fitting the spinodal of the metallic phase in Fig. 2.

Stability of the insulating phase. The insulating phase can be analyzed in a similar fashion but starting from the asymptotic large-Δ_s solution:

$$\begin{aligned} \nu &\approx \Delta_s^{\frac{1}{3}} - (b+2\lambda\phi)\frac{1}{3\Delta_s^{\frac{1}{3}}}, \\ \nu^2 &\approx \Delta_s^{\frac{2}{3}} - \frac{2}{3}(b+2\lambda\phi) + \frac{(b+2\lambda\phi)^2}{9\Delta_s^{\frac{2}{3}}}. \end{aligned}$$

By substituting this back into Eq. (10), we get

$$\begin{aligned} \phi^3 + \phi &= h - \lambda\Delta_s^{\frac{2}{3}} + \lambda\frac{2}{3}(b+2\lambda\phi), \\ \phi^3 + \phi\left(1 - \frac{4}{3}\lambda^2\right) &= h + \lambda\frac{2}{3}b - \lambda\Delta_s^{\frac{2}{3}}, \\ \phi^3 - P\phi &= h + \lambda\frac{2}{3}b - \lambda\Delta_s^{\frac{2}{3}}, \end{aligned}$$

where we have neglected the terms containing inverse powers of Δ_s and introduced $P = 4\lambda^2/3 - 1$.

The insulating phase becomes unconditionally unstable when the right-hand side of the equation reaches the local maximum of the left-hand side. The location of the maximum ϕ_m is easily found from the left-hand side,

$$\phi_m = -\sqrt{\frac{P}{3}}.$$

This results in the following condition for the stability valid in the large Δ_s limit:

$$h + \lambda\frac{2}{3}b - \lambda\Delta_s^{\frac{2}{3}} = \frac{2}{3}\left(\frac{P}{3}\right)^{\frac{3}{2}},$$

from which we get the critical value of Δ_s,

$$\Delta_s^- = \left[\frac{2}{3}b + \frac{h}{\lambda} - \frac{2}{3\lambda}\left(\frac{P}{3}\right)\right]^{\frac{3}{2}}. \tag{B8}$$

Thus, in both the metallic and insulating cases, the scaling of the critical Δ_s is

$$\Delta_s^* \sim (b - b^*)^{\frac{3}{2}} \sim (W - W^*)^{\frac{3}{2}}, \tag{B9}$$

with $\Delta_s^* = \Delta_s^+, \Delta_s^-$ for the metallic and insulating spinodals, respectively. These scalings have been used to fit both boundaries in Fig. 2.

[1] P. Zubko, S. Gariglio, M. Gabay, P. Ghosez, and J.-M. Triscone, Annu. Rev. Condens. Matter Phys. **2**, 141 (2011).

[2] D. B. McWhan, T. M. Rice, and J. P. Remeika, Phys. Rev. Lett. **23**, 1384 (1969).

[3] Y. Tokura, Rep. Prog. Phys. **69**, 797 (2006).

[4] S. Nakatsuji, S. Ikeda, and Y. Maeno, J. Phys. Soc. Jpn. **66**, 1868 (1997).

[5] Q. Han and A. Millis, Phys. Rev. Lett. **121**, 067601 (2018).

[6] J. B. Torrance, P. Lacorre, A. I. Nazzal, E. J. Ansaldo, and C. Niedermayer, Phys. Rev. B **45**, 8209 (1992).

[7] M. L. Medarde, J. Phys.: Condens. Matter **9**, 1679 (1997).

[8] G. Catalan, Phase Transitions **81**, 729 (2008).

[9] S. Catalano, M. Gibert, J. Fowlie, J. Íñiguez, J.-M. Triscone, and J. Kreisel, Rep. Prog. Phys. **81**, 046501 (2018).

[10] S. Middey, J. Chakhalian, P. Mahadevan, J. W. Freeland, A. J. Millis, and D. D. Sarma, Annu. Rev. Mater. Res. **46**, 305 (2016).

[11] J. M. Rondinelli and N. A. Spaldin, Adv. Mater. **23**, 3363 (2011).

[12] A. Demourgues, F. Weill, B. Darriet, A. Wattiaux, J. Grenier, P. Gravereau, and M. Pouchard, J. Solid State Chem. **106**, 330 (1993).

[13] T. Mizokawa, D. I. Khomskii, and G. A. Sawatzky, Phys. Rev. B **61**, 11263 (2000).

[14] S. Johnston, A. Mukherjee, I. Elfimov, M. Berciu, and G. A. Sawatzky, Phys. Rev. Lett. **112**, 106404 (2014).

[15] B. Mandal, S. Sarkar, S. K. Pandey, P. Mahadevan, C. Franchini, A. J. Millis, and D. D. Sarma, arXiv:1701.06819.

[16] I. I. Mazin, D. I. Khomskii, R. Lengsdorf, J. A. Alonso, W. G. Marshall, R. M. Ibberson, A. Podlesnyak, M. J. Martínez-Lope, and M. M. Abd-Elmeguid, Phys. Rev. Lett. **98**, 176406 (2007).

[17] A. Subedi, O. E. Peil, and A. Georges, Phys. Rev. B **91**, 075128 (2015).

[18] P. Seth, O. E. Peil, L. Pourovskii, M. Betzinger, C. Friedrich, O. Parcollet, S. Biermann, F. Aryasetiawan, and A. Georges, Phys. Rev. B **96**, 205139 (2017).

[19] J. Varignon, M. N. Grisolia, J. Íñiguez, A. Barthélémy, and M. Bibes, npj Quantum Mater. **2**, 21 (2017).

[20] H. Park, A. J. Millis, and C. A. Marianetti, Phys. Rev. Lett. **109**, 156402 (2012).

[21] H. Park, A. J. Millis, and C. A. Marianetti, Phys. Rev. B **89**, 245133 (2014).

[22] A. Hampel, P. Liu, C. Franchini, and C. Ederer, npj Quantum Mater. **4**, 5 (2019).

[23] J. Varignon, M. Bibes, and A. Zunger, Nat. Commun. **10**, 1658 (2019).

[24] J. Ruppen, J. Teyssier, I. Ardizzone, O. E. Peil, S. Catalano, M. Gibert, J.-M. Triscone, A. Georges, and D. van der Marel, Phys. Rev. B **96**, 045120 (2017).

[25] K. Haule and G. L. Pascut, Sci. Rep. **7**, 10375 (2017).

[26] K. W. Post, A. S. McLeod, M. Hepting, M. Bluschke, Y. Wang, G. Cristiani, G. Logvenov, A. Charnukha, G. X. Ni, P. Radhakrishnan, M. Minola, A. Pasupathy, A. V. Boris, E. Benckiser, K. A. Dahmen, E. W. Carlson, B. Keimer, and D. N. Basov, Nat. Phys. **14**, 1056 (2018).

[27] J. A. Alonso, M. J. Martínez-Lope, M. T. Casais, J. L. García-Muñoz, M. T. Fernández-Díaz, and M. A. G. Aranda, Phys. Rev. B **64**, 094102 (2001).

[28] Y. Lu, Z. Zhong, M. W. Haverkort, and P. Hansmann, Phys. Rev. B **95**, 195117 (2017).

[29] G. G. Guzmán-Verri, R. T. Brierley, and P. B. Littlewood, arXiv:1701.02318.

[30] A. Mercy, J. Bieder, J. Íñiguez, and P. Ghosez, Nat. Commun. **8**, 1677 (2017).

[31] C. Girardot, J. Kreisel, S. Pignard, N. Caillault, and F. Weiss, Phys. Rev. B **78**, 104101 (2008).

[32] M. K. Stewart, J. Liu, M. Kareev, J. Chakhalian, and D. N. Basov, Phys. Rev. Lett. **107**, 176401 (2011).

[33] J. Ruppen, J. Teyssier, O. E. Peil, S. Catalano, M. Gibert, J. Mravlje, J.-M. Triscone, A. Georges, and D. van der Marel, Phys. Rev. B **92**, 155145 (2015).

[34] S. Prosandeev, L. Bellaiche, and J. Íñiguez, Phys. Rev. B **85**, 214431 (2012).

[35] A. Hampel and C. Ederer, Phys. Rev. B **96**, 165130 (2017).

[36] A. B. Georgescu, O. E. Peil, A. Disa, A. Georges, and A. J. Millis, arXiv:1810.00480.

[37] A. Georges, G. Kotliar, W. Krauth, and M. J. Rozenberg, Rev. Mod. Phys. **68**, 13 (1996).

[38] G. Kotliar, S. Y. Savrasov, K. Haule, V. S. Oudovenko, O. Parcollet, and C. A. Marianetti, Rev. Mod. Phys. **78**, 865 (2006).

[39] S. B. Lee, R. Chen, and L. Balents, Phys. Rev. B **84**, 165119 (2011); Phys. Rev. Lett. **106**, 016405 (2011).

[40] A. Georges, L. D. Medici, and J. Mravlje, Annu. Rev. Condens. Matter Phys. **4**, 137 (2013).

[41] We checked that in all our DMFT calculations the orbital occupation numbers always ended up being nearly equal.

[42] S. Catalano, M. Gibert, V. Bisogni, F. He, R. Sutarto, M. Viret, P. Zubko, R. Scherwitzl, G. A. Sawatzky, T. Schmitt, and J.-M. Triscone, APL Mater. **3**, 062506 (2015).

[43] S. Middey, D. Meyers, M. Kareev, Y. Cao, X. Liu, P. Shafer, J. W. Freeland, J.-W. Kim, P. J. Ryan, and J. Chakhalian, Phys. Rev. Lett. **120**, 156801 (2018).

[44] G. Kotliar, E. Lange, and M. J. Rozenberg, Phys. Rev. Lett. **84**, 5180 (2000).

[45] P. Limelette, A. Georges, D. Jérome, P. Wzietek, P. Metcalf, and J. M. Honig, Science **302**, 89 (2003).

[46] P. E. Blöchl, Phys. Rev. B **50**, 17953 (1994).

[47] G. Kresse and D. Joubert, Phys. Rev. B **59**, 1758 (1999).

[48] G. Kresse and J. Hafner, Phys. Rev. B **47**, 558 (1993).

[49] G. Kresse and J. Furthmüller, Phys. Rev. B **54**, 11169 (1996).

[50] J. P. Perdew, K. Burke, and M. Ernzerhof, Phys. Rev. Lett. **77**, 3865 (1996).

[51] B. J. Campbell, H. T. Stokes, D. E. Tanner, and D. M. Hatch, J. Appl. Crystallogr. **39**, 607 (2006).

[52] J. M. Perez-Mato, D. Orobengoa, and M. I. Aroyo, Acta Crystallogr. A **66**, 558 (2010).

[53] J. A. Alonso, M. J. Martínez-Lope, M. T. Casais, M. A. G. Aranda, and M. T. Fernández-Díaz, J. Am. Chem. Soc. **121**, 4754 (1999).

[54] M. Schüler, O. E. Peil, G. J. Kraberger, R. Pordzik, M. Marsman, G. Kresse, T. O. Wehling, and M. Aichhorn, J. Phys.: Condens. Matter **30**, 475901 (2018).

[55] B. Amadon, F. Lechermann, A. Georges, F. Jollet, T. O. Wehling, and A. I. Lichtenstein, Phys. Rev. B **77**, 205112 (2008).

[56] M. Aichhorn, L. Pourovskii, P. Seth, V. Vildosola, M. Zingl, O. E. Peil, X. Deng, J. Mravlje, G. J. Kraberger, C. Martins, M. Ferrero, and O. Parcollet, Comput. Phys. Commun. **204**, 200 (2016).

[57] O. Parcollet, M. Ferrero, T. Ayral, H. Hafermann, I. Krivenko, L. Messio, and P. Seth, Comput. Phys. Commun. **196**, 398 (2015).

[58] E. Gull, A. J. Millis, A. I. Lichtenstein, A. N. Rubtsov, M. Troyer, and P. Werner, Rev. Mod. Phys. **83**, 349 (2011).

[59] P. Seth, I. Krivenko, M. Ferrero, and O. Parcollet, Comput. Phys. Commun. **200**, 274 (2016).

[60] K. Held, Adv. Phys. **56**, 829 (2007).